Alignment in two-step pulsed laser excitation of Rydberg levels in light atoms: The example of sodium

Keith B. MacAdam* and Michael A. Morrison†
Joint Institute for Laboratory Astrophysics, University of Colorado and National Institute of Standards and Technology, Boulder, Colorado 80309-0440
(Received 8 March 1993)

Aligned atomic Rydberg states of sodium can be prepared using two-step excitation from the ground state by linearly polarized pulsed lasers. Information that is normally inaccessible, e.g., sublevel partial cross sections in charge-transfer experiments, can be obtained when aligned targets are used. The calculations of orbital alignment must carefully allow for fine and hyperfine structure, laser linewidths, pulse widths and delays, sublevel coherences, and other factors. In this paper we derive the orbital alignments and time-averaged d-state sublevel populations for $3\,^2S_{1/2}\rightarrow 3\,^2P_{J_1}\rightarrow n\,^2D$ excitations in Na using angular-momentum and density-matrix methods. We consider both quadrupole alignment $A^{(2)}$ and hexadecapole alignment $A^{(4)}$, with excitation through either $J_1=\frac{1}{2}$ or $\frac{3}{2}$ intermediate states considered on the same footing. We show sublevel populations for $|M_L|=0$, 1, and 2 analytically and graphically. Finally, we formulate the experimental design problem quantitatively in order to ascertain how to optimize the choice of polarizer angles for extraction of sublevel partial cross sections. Although perhaps the commonest instance, two-step excitation of Na(nd) is but one of a large number of interesting cases, and this study is further intended to illustrate and guide the application of these methods to other light atoms.

PACS number(s): 32.80.Rm, 34.60.+z, 34.50.Pi

I. INTRODUCTION

One of the earliest and most widely used techniques for modern Rydberg atom studies is two-step excitation of an atomic beam or vapor by pulsed lasers [1–4]. The sodium atom, with its convenient arrangement of energy levels, its quasi-one-electron structure, and its ease of use in the laboratory, has received more attention than any other element in Rydberg studies of all sorts. These studies range from spectroscopy [5,6] to collisions [7–12] (at energies from subthermal to MeV) to cavity quantum electrodynamics [13,14] to wave-packet studies [15] to quantum manifestations of classical chaos [16]. The most common two-step excitation scheme for populating high-lying nd states [1] is

$$\mathrm{Na}(3\,^2S_{1/2})\xrightarrow[h\nu_1]{}\mathrm{Na}(3\,^2P_{1/2,3/2})\xrightarrow[h\nu_2]{}\mathrm{Na}(n\,^2D_{3/2,5/2})\ , \qquad (1)$$

where the wavelength $\lambda_1=c/\nu_1=589.6$ or 589.0 nm for the $3\,^2P_{1/2}$ or $3\,^2P_{3/2}$ intermediate state, respectively, and $\lambda_2=c/\nu_2=417$–408 nm, for n ranging from $n=15$ to infinity. Of course, one can also populate $n\,^2S_{1/2}$ by this scheme, and, via a small Stark-mixing electric field, $n\,^2P_{1/2,3/2}$ as well [3]. By more complex schemes one can even populate individual parabolic levels or circular states [17,18].

In the early 1970s the first known studies of alignment and orientation in atomic collisions were undertaken [19,20]. Alignment and orientation refer to even-order and odd-order multipole moments, respectively, of atomic angular momentum [21]. These multipole moments may be produced by anisotropic scattering processes, and, conversely, the alignment and orientation of a prepared target may affect the outcome of scattering events. In particular, *orientation* refers to a net circulation in the atom or (in lowest order) to a nonzero value of $\langle \mathbf{J} \rangle$ for the system; this arises from an imbalance in the populations of sublevels with magnetic quantum numbers $+M_L$ and $-M_L$. By contrast, *alignment* refers to a nonuniform population of sublevels with various values of $|M_L|$ (regardless of sign) and is proportional to even multipoles of the atom: in the present study, the quadrupole and hexadecapole moments are of interest (see Sec. II D).

The 20 years since those initial studies of alignment and orientation have seen a vast growth in this research area, which now includes electron-atom [22], atom-atom [23], ion-atom [24], and even molecular processes [25]. Fano and Macek [26] first placed the description of alignment and orientation in atomic physics on a firm theoretical foundation. Experimental investigation of the alignment produced by collisions and of the effect of target alignment on collision cross sections began with the e-He coincidence experiments of Eminyan *et al.* [27] and the e-Na superelastic experiments of Hertel and Stoll [28]. Andersen, Gallagher, and Hertel [29] have thoroughly reviewed orientation and alignment in electron-atom collisions, and further reviews are now in preparation [30].

Recent measurements of charge-transfer (CT) cross sections for collisions of singly charged ions with Na Rydberg atoms [31], e.g.,

$$\mathrm{Na}^+ + \mathrm{Na}(nd)\rightarrow \mathrm{Na}(n'l') + \mathrm{Na}^+\ , \qquad (2)$$

have revealed that the cross section σ^{CT} for capture into

all bound states $(n'l')$ of the projectile can be varied by as much as 10% (particularly near certain velocities less than that of the orbiting electron) by rotating the plane of linear polarization of the ν_2 laser about an axis perpendicular to the momentum of the incident projectile beam [32]. Because the deflection of the projectile in such a Rydberg-atom collision is negligible, these processes offer little hope for experiments that define the collision plane, as required for the study of initial-state orientation [33,34]. All neutralized Rydberg-state projectiles Na$(n'l')$ are collected and detected regardless of impact parameter or final-state quantum numbers. Thus only target *alignment* can affect the measured cross section. Such alignments are established in the Na(nd) target by the directions and polarizations of the two exciting lasers, subject to constraints imposed by angular-momentum coupling and the properties of the relevant electric dipole operators.

One can represent dynamical information about the initially aligned state either in terms of the density matrix, which describes the populations and coherences of the nd sublevels [35,36], or the alignment tensors, which are the mean multipole moments of the angular momentum in the aligned state [21]. The total charge-transfer cross section for process (2) can be written in terms of either elements of the density matrix or components of the alignment tensors,

$$\sigma^{\mathrm{CT}}=\sum_i p_i\sigma_i^{\mathrm{CT}}=\sum_k A_0^{(k)}\sigma_{(k)}^{\mathrm{CT}}\ , \tag{3}$$

where p_i is the fractional population of the ith magnetic sublevel of the nd state (e.g., one of the allowed $M_L=-2,-1,\ldots,1,2$ sublevels) as represented by the ith diagonal element of the appropriate density matrix, and σ_i^{CT} is the partial cross section of the ith sublevel. Similarly, $A_0^{(k)}$ is the kth-rank target alignment tensor and $\sigma_{(k)}^{\mathrm{CT}}$ is the corresponding partial cross section. The sums run over all relevant sublevels i or tensor ranks k. Note that although sublevel coherences (off-diagonal density-matrix elements) and alignment components $A_q^{(k)}$ for $q\neq 0$ may exist, they do not appear in Eq. (3) because the collision and detection processes in the Rydberg experiment impose a cylindrical symmetry that precludes their contributing to the charge transfer cross section.

In this paper we exhibit the theory by which one can use laser polarizations and a mutually perpendicular excitation and collision geometry to obtain sublevel populations and alignment components experimentally. We also show how to optimize the experimental design for measurement of the sublevel cross sections or kth-rank partial cross sections. The theory, which is based on density matrices [35], is closely related to the determination of alignment in laser-induced fluorescence [37]. Although we have simplified its implementation by approximations that are valid for many contemporary Rydberg-atom experiments, the framework presented here should serve as a structure upon which one could erect a more comprehensive theory, encompassing hyperfine effects [38], quantum beats [1,39], circular polarization, orientation, and higher-order alignments.

In Sec. II we derive exact expressions for diagonal density-matrix elements and alignments for the two-step excitation in Eq. (1). We then display these results in Sec. III and we use them to discuss experimental design and optimization in Sec. IV. In Sec. V we summarize the present explicit results and compare them to the only comparable previous analysis of which we are aware, a different experimental context that simplifies the present problem to three special cases.

II. THEORY

A. Excitation scheme and experimental geometry

Figure 1 shows the two-step excitation scheme and the hyperfine [38] and fine structure [39] of the $3\,^2P$ and $n\,^2D$ levels. The initial $3\,^2S_{1/2}$ ground state is unpolarized, so we shall describe this excitation quantum mechanically using density matrices. The first excitation uses a pulsed laser of frequency ν_1 whose linewidth ($\Delta\lambda_1\gtrsim 0.1$ Å, $\Delta\nu_1\gtrsim 10$ GHz) overlaps all components of the $3\,^2S\rightarrow 3\,^2P_{J_1}$ hyperfine multiplet (where J_1 is the total electronic angular-momentum quantum number of the intermediate $3\,^2P$ level). This linewidth does, however, resolve the fine-structure splitting of 520 GHz between levels with $J_1=\frac{1}{2}$ or $\frac{3}{2}$. Linearly polarized lasers do not optically pump hyperfine levels, but because the oscillator strength of the $3s\rightarrow 3p$ line is very large, some degree of saturation may occur [40]. This has the effect of shortening the time an atom spends in the $3\,^2P$ state, preventing some hyperfine depolarization [21,26,35] that might occur were the atom not promptly excited to the nd state. The laser pulse widths range from 5 to 8 ns, typical of yttrium-aluminum-garnet- (YAG) pumped dye lasers, and the delay between the first and second laser pulses ranges from 0 to 5 ns.

The second excitation, from the $3\,^2P_{J_1}$ level to the nd Rydberg state, uses a similar pulsed laser whose linewidth overlaps all hyperfine components of $3\,^2P_{J_1}$ *and* the fine and hyperfine components of the nd state, thereby exciting both fine-structure levels of the Rydberg state. So while the first laser excites the atom from a particular initial level ($J_0=\frac{1}{2}$) to a particular intermediate level $3\,^2P_{J_1}$,

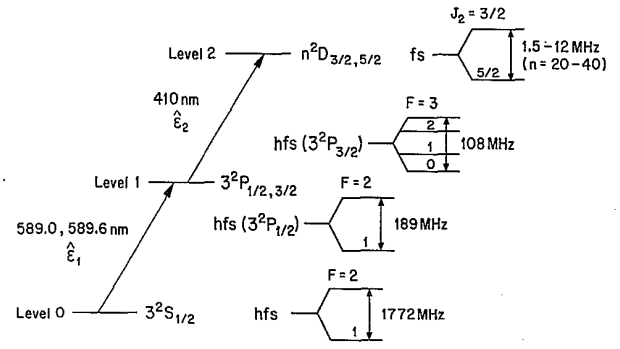

FIG. 1. The sodium $3s$, $3p$, and nd (Rydberg) energy levels and fine and hyperfine structure for the present two-step laser-excitation scheme.

the second laser, if incident on an atom in the $3\,^2P_{3/2}$ state, effectively averages over the two allowed final-state values $J_2=\frac{3}{2},\frac{5}{2}$. Of course, if the atom is in the $3\,^2P_{1/2}$ intermediate state, the electric dipole selection rule $\Delta J=0,\pm1$ permits only excitation of $n\,^2D_{3/2}$.

Under these conditions, we can completely neglect hyperfine structure. The largest $\Delta F=1$ or 2 splitting of the $3\,^2P_{3/2}$ level is 93 MHz [38]. Therefore hyperfine quantum beats [26] in $3\,^2P_{3/2}$ will occur at frequencies $\nu\leq 93$ MHz, i.e., with periods longer than $T=11$ ns. The short pulse widths and pulse separation, together with saturation effects, imply that the sodium atoms will reside in the $3\,^2P_{3/2}$ level for much less than one period T, so we can neglect hyperfine depolarization for $J_1=\frac{3}{2}$. The other intermediate state, with $J_1=\frac{1}{2}$, is marginal in this respect. The $F=1$ and 2 sublevels of this term are separated by 188.6 MHz, so the beat period is $T=5$ ns. Although some hyperfine depolarization may occur, it will be reduced by saturation in the first (589.6 nm) excitation. In the final *nd* Rydberg state, hyperfine splittings are on the order of kHz and may be neglected completely. These conditions, therefore, justify use of a *fine-structure coupled representation,* in which we identify the initial ($i=0$), intermediate ($i=1$), and final ($i=2$) states discussed above by $|L_iS_iJ_iM_i\rangle$ in determining the density matrix.

Figure 2 shows the geometry of a typical experiment [32]. The Na atomic beam (not shown) approaches the origin in the $+\hat{\mathbf{x}}$ direction, and two laser beams with frequencies ν_1 and ν_2 approach in the $-\hat{\mathbf{x}}$ and $+\hat{\mathbf{y}}$ directions, respectively. We take the axis of the projectile (ion) beam $+\hat{\mathbf{z}}$ as the axis of quantization; this is also the axis of cylindrical symmetry of the collision and detection. This choice facilitates describing the excitation and subsequent collision in terms of alignment tensors $A_q^{(k)}$, since only $q=0$ components contribute to the cylindrically averaged signal, and we can express these tensors solely in terms of *diagonal* elements of the *nd* density matrix. (Additionally, reflection symmetry in the plane normal to this axis implies that only even-k tensors are nonzero and that the excitation cannot induce an imbalance in the orbital magnetic sublevels, i.e., a nonzero orientation.) The key quantities in deriving the density matrix are β_1 and β_2, the angles of the vectors $\hat{\boldsymbol{\epsilon}}_1$ and $\hat{\boldsymbol{\epsilon}}_2$ of (electric field) linear polarization of the laser beams. With the present geometry, the polarization vector for the first laser is in the xz plane and that of the second is in the yz plane. For either laser $\beta_i=0$ corresponds to polarization parallel to $\hat{\mathbf{z}}$.

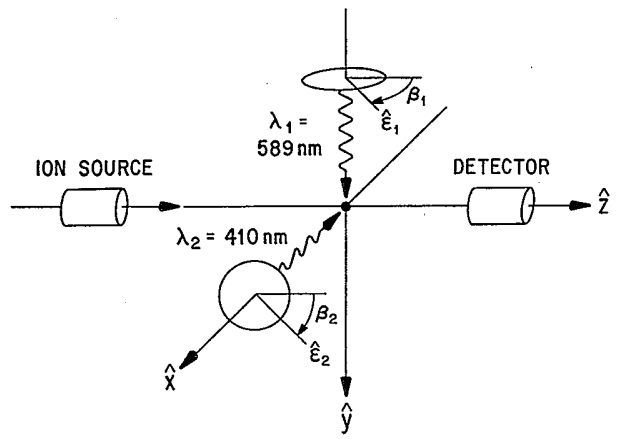

FIG. 2. The mutually perpendicular laser excitation, polarization, and collision geometry for experiments analyzed in Sec. II.

B. The density matrix in the total angular-momentum basis

To obtain an expression for the density operator for the *nd* state we begin with the unnormalized density operator for the (unpolarized) ground state

$$\hat{\rho}^{3s}=\sum_{M_0}|\tfrac{1}{2}M_0\rangle\langle\tfrac{1}{2}M_0|=\hat{P}_0\ , \tag{4}$$

where we label atomic kets by the quantum numbers of the total electronic angular momentum and its projection on the quantization axis. Thus $|\frac{1}{2}M_0\rangle$ represents the sublevel of the $3\,^2S_{1/2}$ ground state with $\langle J_z\rangle=M_0$, and the sum runs over $M_0=-\frac{1}{2},+\frac{1}{2}$. We also note that this density operator is just equal to the projection operator $\hat{P}_0$ onto the electronic ground state.

The density operator for the $3p$ state that results from the first step of excitation is

$$\hat{\rho}^{3p}=\hat{T}_1\hat{\rho}^{3s}\hat{T}_1^{\dagger}\ , \tag{5}$$

where $\hat{T}_1$ is the electric dipole transition operator [41] for the transition to $3\,^2P_{J_1}$ via ν_1 light polarized along $\hat{\boldsymbol{\epsilon}}_1$,

$$\hat{T}_1=\sum_{M_1}|J_1M_1\rangle\langle J_1M_1|(\hat{\boldsymbol{\epsilon}}_1\cdot\hat{\mathbf{r}})=\hat{P}_1(\hat{\boldsymbol{\epsilon}}_1\cdot\hat{\mathbf{r}})\ . \tag{6}$$

Because the first excitation could excite various sublevels of the $3\,^2P_{J_1}$ state, this operator requires a sum over sublevels, $-J_1\leq M_1\leq J_1$. The operator $\hat{\mathbf{r}}$ corresponds to the spatial coordinate of the valence electron in Na, and $\hat{P}_1$ is the projection operator onto the $3\,^2P_{J_1}$ state.

We describe the second excitation similarly, via the transition operator

$$\hat{T}_2=\sum_{J_2}\sum_{M_2}|J_2M_2\rangle\langle J_2M_2|(\hat{\boldsymbol{\epsilon}}_2\cdot\mathbf{r})=\hat{P}_2(\hat{\boldsymbol{\epsilon}}_2\cdot\mathbf{r})\ , \tag{7}$$

where in order to allow for excitation of both *nd* fine-structure levels we sum over J_2 as well as M_2. So $\hat{P}_2$ is the projection operator onto the *nd* Rydberg state. The density operator of this state is, finally,

$$\hat{\rho}^{nd}=\hat{T}_2\hat{\rho}^{3p}\hat{T}_2^{\dagger}=\hat{T}_2\hat{T}_1\hat{\rho}^{3s}\hat{T}_1^{\dagger}\hat{T}_2^{\dagger}\ . \tag{8}$$

Note that the transition operators do not preserve normalization; so, for example, to normalize $\hat{\rho}^{nd}$ we must divide by its trace.

In the $|J_2M_2\rangle$ representation, the matrix elements of $\hat{\rho}^{nd}$, the elements of the density matrix, are simply

$$\rho^{nd}_{J_2M_2,J_2'M_2'}=\langle J_2M_2|\hat{R}|J_2'M_2'\rangle\ , \tag{9}$$

where for convenience we have introduced the effective transition operator

$$\hat{R} \equiv (\hat{\epsilon}_2 \cdot \hat{\mathbf{r}}) \hat{P}_1 (\hat{\epsilon}_1 \cdot \hat{\mathbf{r}}) \hat{P}_0 (\hat{\epsilon}_1^* \cdot \hat{\mathbf{r}}) \hat{P}_1' (\hat{\epsilon}_2^* \cdot \hat{\mathbf{r}}) \ . \tag{10}$$

To avoid confusion we have identified the second projection operator onto the $3\,^2P_{J_1}$ level in (10) with a prime,

$$\hat{P}_1' = \sum_{M_1'} |J_1 M_1' \rangle \langle J_1 M_1'| \ . \tag{11}$$

We are interested in the *orbital* angular-momentum properties of the *nd* state as it participates in the collision and so will ultimately require a (reduced) density matrix in an *uncoupled* angular-momentum representation. We first simplify the full density matrix using tensor methods [42].

A similar simplification arises in the study of laser-induced fluorescence (LIF), a technique for examining the properties of a collisionally aligned state by excitation to a higher state, followed by analysis of polarized emission to a lower state. In their theoretical treatment of LIF, Greene and Zare [37] encountered an operator similar to $\hat{R}$ and wrote it in terms of contracted polarization tensors. Following this approach we first contract the spherical tensor operators (STO's) corresponding to the polarization vectors for the two steps of excitation, $\hat{\epsilon}_1$ and $\hat{\epsilon}_2$ to form the 2^k multipole moments of the radiation of the first or second laser pulse,

$$\hat{E}_q^{(k)}(\hat{\epsilon}_i, \hat{\epsilon}_i^*) \equiv [\hat{\epsilon}_i^{(1)} \otimes \hat{\epsilon}_i^{(1)*}]_q^{(k)} \ , \tag{12}$$

where $\hat{\epsilon}_i^{(1)}$ is the STO for either the first ($i=1$) or second ($i=2$) step and the superscript (1) indicates that these are first-rank STO's.

To introduce these contracted polarization tensors into the density matrix (9) we must rearrange the constituents of the effective transition operator $\hat{R}$ so as to group together pairs corresponding to the same excitation step. The tensorial properties of $\hat{R}$ under rotations are unaffected by the projection operators, which are rotational scalars, although of course we must keep track of them throughout the analysis. Thus the symmetries of $\hat{R}$ are the same as those of the simpler operator

$$\hat{Q} = (\hat{\epsilon}_2 \cdot \hat{\mathbf{r}}_1)(\hat{\epsilon}_1 \cdot \hat{\mathbf{r}}_2)(\hat{\epsilon}_1^* \cdot \hat{\mathbf{r}}_3)(\hat{\epsilon}_2^* \cdot \hat{\mathbf{r}}_4) \ , \tag{13}$$

where following Zare [21] we have temporarily labeled the STO's corresponding to the radial coordinate $\mathbf{r}$ by indices ($i=1,\ldots,4$) that denote the factor in which each appears. By writing the dot products in (13) as tensor contractions we can rewrite $\hat{Q}$ in terms of a further contraction of the two contracted tensors defined in Eq. (12),

$$\hat{\mathcal{E}}_q^{(k)}(k_1,k_2) \equiv [\hat{E}^{(k_1)}(\hat{\epsilon}_1, \hat{\epsilon}_1^*) \otimes \hat{E}^{(k_2)}(\hat{\epsilon}_2, \hat{\epsilon}_2^*)]_q^{(k)} \ , \tag{14}$$

and a similar multiple contraction of the spatial coordinates in (13). The latter operator is a contraction of the form

$$\hat{R}^{(k)}(i,j) = [\hat{r}_i^{(1)} \otimes \hat{r}_j^{(1)}]^{(k)} \ . \tag{15}$$

In particular, by recoupling [37] the STO's in $\hat{Q}$ so as to form the groupings in Eqs. (12) and (15) we can rewrite $\hat{Q}$ as

$$\hat{Q} = \sum_{k_1,k_2,k,q} (-1)^{k-q} \hat{\mathcal{E}}_q^{(k)}(k_1,k_2) \times [\hat{R}^{(k_1)}(2,3) \otimes \hat{R}^{(k_2)}(1,4)]_{-q}^{(k)} \tag{16}$$

and the *nd* density matrix in the $|J_2 M_2\rangle$ basis (9) as

$$\rho^{nd}_{J_2M_2,J_2'M_2'} = \sum_{k_1,k_2} \sum_{k,q} (-1)^{k-q} \hat{\mathcal{E}}_q^{(k)}(k_1,k_2) \langle J_2 M_2 | [\hat{R}^{(k_1)}(2,3) \otimes \hat{R}^{(k_2)}(1,4)]_{-q}^{(k)} \hat{P}_1 \hat{P}_0 \hat{P}_1' | J_2' M_2' \rangle \ . \tag{17}$$

The intertwining of the projection operators with the coordinate STO's in (17) is obscured by the tensor notation, but the actual form of the operator is treated by Greene and Zare [37]. The dependence of these matrix elements on the polarizer angles β_1 and β_2 arises from the presence of the single-photon tensors $\hat{E}^{(k_i)}(\hat{\epsilon}_i, \hat{\epsilon}_i^*)$ in $\hat{\mathcal{E}}_q^{(k)}(k_1,k_2)$ and appears as Legendre polynomials when these tensors are referred to the quantization axis of the collision frame.

Evaluation of the contracted polarization tensors $\hat{E}^{(k_i)}$ ($i=1,2$) of Eq. (12) is particularly simple in a reference frame whose quantization axis is along $\hat{\epsilon}_i$. In such a frame the spherical components of the (real) linear polarization vector are $\hat{\epsilon}_{0,i}^{(1)}=1$ and $\hat{\epsilon}_{\pm 1,i}^{(1)}=0$. Hence each contracted tensor is just

$$\hat{E}_q^{(k_i)} = \sqrt{2k_i+1} \begin{bmatrix} 1 & 1 & k_i \\ 0 & 0 & 0 \end{bmatrix} \delta_{q,0} \quad (i=1,2) \ . \tag{18}$$

Thus $\hat{E}^{(1)}$ vanishes identically, which also must be true in the collision frame. Therefore k_1 and k_2 assume values 0 and 2 only, and the rank of the multiply contracted tensors in (14) is restricted to $k=0$, 2, and 4. By rotating $\hat{E}_{q_1}^{(k_1)}(\hat{\epsilon}_1, \hat{\epsilon}_1^*)$ and $\hat{E}_{q_2}^{(k_2)}(\hat{\epsilon}_2, \hat{\epsilon}_2^*)$ into the collision frame we obtain an expression for the multiply contracted tensor Eq. (14) for $q=0$ in terms of spherical harmonics of the polarizer angle:

$$\hat{\mathcal{E}}_0^{(k)}(k_1,k_2) = 4\pi \sum_{q_1,q_2} (-1)^{k_1-k_2} (2k+1)^{1/2} \times \begin{bmatrix} k_1 & k_2 & k \\ q_1 & q_2 & 0 \end{bmatrix} \begin{bmatrix} 1 & 1 & k_1 \\ 0 & 0 & 0 \end{bmatrix} \times \begin{bmatrix} 1 & 1 & k_2 \\ 0 & 0 & 0 \end{bmatrix} \times Y_{k_1}^{q_1}(\beta_1,0) Y_{k_2}^{q_2}(\beta_2,\pi/2) \ . \tag{19}$$

These quantities depend in general on β_1 and β_2, because the quantization axes of the two constituent STO's in (14) are not coincident. This general expression reduces to the simplified analytical results of Table I [37].

The density matrix ρ^{nd} contains information about the mixture of the orbital magnetic (M_2) sublevels of the *nd* Rydberg state at $t=0$, after the second step of excitation. As time passes this matrix evolves according to the time-evolution operator as

$$\rho^{nd}_{J_2M_2,J_2'M_2'}(t)=\exp\{i[E(J_2)-E(J_2')]t/\hbar\} \times\rho^{nd}_{J_2M_2,J_2'M_2'}(0)\ , \tag{20}$$

where $E(J_2)$ is the energy of the J_2 fine-structure level of the *nd* state. The matrix elements of ρ^{nd} that are off diagonal in J_2 therefore represent time-dependent sublevel coherences that oscillate at a frequency corresponding to the *nd* fine-structure separation.

But in the charge-transfer experiment (2) the Na(*nd*) ensemble that is populated by two-step pulsed-laser excitation is used as a collision target for 3 or 4 μs, after which time the excited atoms drift with the atomic beam in the $\hat{\mathbf{x}}$ direction beyond the region of overlap with the $\hat{\mathbf{z}}$-directed ion beam. Charge-transfer products are subsequently collected downstream over a corresponding interval without time resolution. Therefore it is appropriate to use the *time-averaged* density matrix $\bar{\rho}^{nd}$ to represent the target ensemble in such experiments. Because the averaging interval extends over several cycles of the *nd* fine-structure frequency [at least for values of n up to about $n=50$, at which point the Na(*nd*) fine-structure splitting $\Delta E/h$ becomes less than 1 MHz], the off-diagonal elements of this matrix between $J_2=\frac{3}{2}$ and $\frac{5}{2}$ average to zero, making $\bar{\rho}^{nd}$ block diagonal with respect to J_2. So henceforth we shall be concerned only with elements $\bar{\rho}^{nd}_{J_2M_2,J_2M_2'}$ of this time-averaged matrix.

To simplify this matrix, we use the Wigner-Eckart theorem [21] to write the matrix element of the contracted coordinate tensors (15) in terms of the absorption line strengths for the two steps of the excitation, $|\langle 3\,^2S_{1/2}\|\hat{r}^{(1)}\|3\,^2P_{J_1}\rangle|^2$ and $|\langle 3\,^2P_{J_1}\|\hat{r}^{(1)}\|n\,^2D_{J_2}\rangle|^2$. This yields for the J_2 block of the time-averaged density matrix

$$\bar{\rho}^{nd}_{J_2M_2,J_2M_2'}=(-1)^{J_2-M_2}\sum_{k_1,k_2}\sum_{k,q}(-1)^{k-q+J_1+3/2}[(2k_1+1)(2k_2+1)(2k+1)]^{1/2}\hat{\mathcal{E}}^{(k)}_q(k_1,k_2) \times\begin{pmatrix} J_2 & k & J_2\\ -M_2 & -q & M_2'\end{pmatrix}\begin{Bmatrix} J_1 & J_1 & k_1\\ 1 & 1 & \frac{1}{2}\end{Bmatrix}\begin{Bmatrix} J_1 & 1 & J_2\\ J_1 & 1 & J_2\\ k_1 & k_2 & k\end{Bmatrix} \times|\langle 3\,^2S_{1/2}\|\hat{r}^{(1)}\|3\,^2P_{J_1}\rangle|^2|\langle 3\,^2P_{J_1}\|\hat{r}^{(1)}\|n\,^2D_{J_2}\rangle|^2\ , \tag{21}$$

where we have used the results of Greene and Zare to simplify the matrix elements in (17) [37].

C. The reduced density matrix in the orbital angular-momentum basis

In the experimental context described in Sec. I, electron spin plays no direct role; in the charge-transfer experiments (2), for example, we seek the *spatial* characteristics of the target *nd* state and the corresponding sublevel partial cross sections $\sigma^{\rm CT}_{M_L}$ in Eq. (3). Therefore, since we are interested in the *orbital* populations and alignment properties of the *nd* Rydberg state and do not measure its spin properties, we must uncouple $\hat{\mathbf{L}}$ and $\hat{\mathbf{S}}$ in $\bar{\rho}^{nd}$ and then construct the appropriate reduced density matrix [35] by forming a trace with respect to the unmeasured spin observables.

In the reduced matrix elements in Eq. (21) $\hat{r}^{(1)}$ acts only on the variables in the space in which $\hat{\mathbf{L}}$ acts, not the spin space. So we can simplify the tensor contractions in these matrix elements, uncoupling the angular momenta to obtain

TABLE I. Contraction of the polarization vectors for a two-step laser excitation of an *nd* Rydberg state of Na, Eq. (19).

$\hat{\mathcal{E}}^{(0)}_0(0,0)$	$\frac{1}{3}$
$\hat{\mathcal{E}}^{(2)}_0(2,0)$	$\frac{1}{3\sqrt{2}}(1-3\cos^2\beta_1)$
$\hat{\mathcal{E}}^{(2)}_0(0,2)$	$\frac{1}{3\sqrt{2}}(1-3\cos^2\beta_2)$
$\hat{\mathcal{E}}^{(0)}_0(2,2)$	$\frac{1}{6\sqrt{5}}[1-3(\cos^2\beta_1+\cos^2\beta_2-3\cos^2\beta_1\cos^2\beta_2+\sin^2\beta_1\sin^2\beta_2)]$
$\hat{\mathcal{E}}^{(2)}_0(2,2)$	$-\frac{1}{3\sqrt{14}}[1-3(\cos^2\beta_1+\cos^2\beta_2-3\cos^2\beta_1\cos^2\beta_2-\sin^2\beta_1\sin^2\beta_2)]$
$\hat{\mathcal{E}}^{(4)}_0(2,2)$	$\frac{1}{\sqrt{280}}[2-6(\cos^2\beta_1+\cos^2\beta_2-3\cos^2\beta_1\cos^2\beta_2)-\sin^2\beta_1\sin^2\beta_2]$

$$\langle 3\,^2S_{1/2}\|\hat{r}^{(1)}\|3\,^2P_{J_1}\rangle = (-1)^{J_1+3/2}[2(2J_1+1)]^{1/2}\begin{Bmatrix} 0 & \frac{1}{2} & \frac{1}{2} \\ J_1 & 1 & 1 \end{Bmatrix} \times\langle 3s\|\hat{r}^{(1)}\|3p\rangle\,, \tag{22a}$$

$$\langle 3\,^2P_{J_1}\|\hat{r}^{(1)}\|n\,^2D_{J_2}\rangle = (-1)^{J_2+5/2}[(2J_1+1)(2J_2+1)]^{1/2} \times\begin{Bmatrix} 1 & J_1 & \frac{1}{2} \\ J_2 & 2 & 1 \end{Bmatrix}\langle 3p\|\hat{r}^{(1)}\|nd\rangle\,. \tag{22b}$$

To transform the time-averaged density matrix from the coupled to the uncoupled angular-momentum basis, we apply the Clebsch-Gordan series. We then form the reduced density matrix taking the trace of the uncoupled time-averaged density matrix as

$$\bar{\rho}^{nd}_{M_L,M_L'} = \sum_{M_S} \bar{\rho}^{nd}_{M_L M_S, M_L' M_S}\,, \tag{23}$$

where all projection quantum numbers refer to the *nd* state with $L=2$ and $S=\frac{1}{2}$. But to analyze the Rydberg state in the collision frame we require only the *diagonal* elements of the reduced density matrix—those for $M_L=M_L'$. The relationship of these elements to the average density matrix (21) is therefore

$$\bar{\rho}^{nd}_{M_L,M_L} = \sum_{M_S,M_2}\sum_{J_2}(2J_2+1)\begin{pmatrix} 2 & \frac{1}{2} & J_2 \\ M_L & M_S & -M_2 \end{pmatrix}^2 \times\bar{\rho}^{nd}_{J_2M_2,J_2M_2}\,. \tag{24}$$

Note that $M_2=M_L+M_S$, a consequence of the $3j$ symbol in this result. Furthermore, since we require only $M_2'=M_2$ we may set $q=0$ in (17) and drop the summation over q.

Evaluation of the result of substituting $\bar{\rho}^{nd}_{J_2M_2,J_2M_2}$ from Eq. (21) into Eq. (24) is facilitated by the identity [43]

$$\sum_{M_S,M_2}(-1)^{1/2-M_S}\begin{pmatrix} 2 & \frac{1}{2} & J_2 \\ M_L & M_S & -M_2 \end{pmatrix}^2\begin{pmatrix} J_2 & k & J_2 \\ -M_2 & 0 & M_2 \end{pmatrix} = (-1)^{k+1}\begin{pmatrix} 2 & k & 2 \\ -M_L & 0 & M_L \end{pmatrix}\begin{Bmatrix} 2 & k & 2 \\ J_2 & \frac{1}{2} & J_2 \end{Bmatrix}. \tag{25}$$

Our final result for the diagonal elements of the reduced time-averaged density matrix for the *nd* Rydberg state resulting from two-step excitation is

$$\bar{\rho}^{nd}_{M_L,M_L} = (-1)^{M_L}\tfrac{1}{3}|\langle 3s\|\hat{r}^{(1)}\|3p\rangle|^2 \times|\langle 3p\|\hat{r}^{(1)}\|nd\rangle|^2 \times\sum_{k_1,k_2}\sum_{k}\begin{pmatrix} 2 & k & 2 \\ -M_L & 0 & M_L \end{pmatrix}\hat{\mathcal{E}}_0^{(k)}(k_1,k_2) \times f(k_1k_2k;J_1)\,, \tag{26}$$

where we have gathered the kinematic factors resulting from angular-momentum coupling in the numerical factor

$$f(k_1k_2k;J_1) = (-1)^{J_1+3/2}(2J_1+1)^2[(2k_1+1)(2k_2+1)(2k+1)]^{1/2}\begin{Bmatrix} J_1 & J_1 & k_1 \\ 1 & 1 & \frac{1}{2} \end{Bmatrix} \times\sum_{J_2=\frac{3}{2}}^{5/2}(-1)^{J_2+1/2}(2J_2+1)^2\begin{Bmatrix} J_2 & k & J_2 \\ 2 & \frac{1}{2} & 2 \end{Bmatrix}\begin{Bmatrix} J_2 & J_1 & 1 \\ 1 & 2 & \frac{1}{2} \end{Bmatrix}^2\begin{Bmatrix} J_1 & 1 & J_2 \\ J_1 & 1 & J_2 \\ k_1 & k_2 & k \end{Bmatrix}. \tag{27}$$

For convenience, we present values of these factors for $J_1=\frac{1}{2}$ and $\frac{3}{2}$ in Table II and analytical forms for the resulting density matrix elements in Table III.

The diagonal elements in Table III are proportional to the populations in the orbital magnetic sublevels of the *nd* state. These sublevels, labeled by M_L, are defined with respect to the $\hat{z}$ quantization axis of the collision frame. As expected, Eq. (26) shows the populations for $+M_L$ and $-M_L$ to be equal. To obtain the corresponding *normalized* density matrix we divide $\bar{\rho}^{nd}$ by its trace,

$$\mathrm{Tr}(\bar{\rho}^{nd}) = \frac{\sqrt{5}}{3}\sum_{k_1,k_2}\hat{\mathcal{E}}_0^{(0)}(k_1,k_2)f(k_1,k_2,0;J_1) \times|\langle 3s\|\hat{r}^{(1)}\|3p\rangle|^2 \times|\langle 3p\|\hat{r}^{(1)}\|nd\rangle|^2\,, \tag{28}$$

which (up to an overall constant) represents the *total* population of the Na(nd) state produced by the two-step excitation. Analytical expressions for the trace also appear in Table III.

D. Alignment tensors

The alignment tensors $A_q^{(k)}$ describe the distribution of Rydberg atoms among the available magnetic sublevels in this state, $|M_L|=0$, 1, and 2. As noted above, the axial symmetry of the time-averaged *nd* population in the collision frame implies that only the $q=0$ components of these tensors contribute to the experimental cross section. Similarly, reflection symmetry in the plane normal to the quantization axis implies that only alignment tensors of even rank k are nonzero. Finally, the $3j$ symbol in the

TABLE II. Angle-independent kinematic functions Eq. (27) for the reduced time-averaged density matrix of Eq. (26).

(k_1,k_2) \ k	0	2	4
		$J_1=\frac{1}{2}$	
(0,0)	$\frac{2\sqrt{5}}{45}$	0	0
(0,2)	0	$\frac{\sqrt{35}}{45}$	0
(2,0)	0	0	0
(2,2)	0	0	0
		$J_1=\frac{3}{2}$	
(0,0)	$\frac{4\sqrt{5}}{45}$	0	0
(0,2)	0	$\frac{32\sqrt{35}}{1125}$	0
(2,0)	0	$\frac{32\sqrt{35}}{1125}$	0
(2,2)	$\frac{1}{45}$	$-\frac{22\sqrt{5}}{1125}$	$\frac{6}{25}$

tensor contraction (19) for $\mathcal{E}_q^{(k)}(k_1,k_2)$ prescribes the triangle rule $\Delta(k_1k_2k)$, which restricts the rank of this polarization tensor—and hence of the alignment tensor—to $k=0$, 2, and 4. The alignments reflected in the nonzero tensors $A_0^{(k)}$ represent inequalities in the populations $p_{|M_L|}$ and $p_{|M_L'|}$ for $|M_L|\neq|M_L'|$.

TABLE III. Explicit expressions for the trace and diagonal elements of the unnormalized reduced time-averaged density matrix evaluated from Eqs. (28) and (26), respectively.

J_1	$\mathrm{Tr}(\bar{\rho}^{nd})$
1/2	$\frac{2}{81}$
3/2	$\frac{1}{1620}[79+3(\cos2\beta_1+\cos2\beta_2+\cos2\beta_1\cos2\beta_2)]$

$J_1=\frac{1}{2}$

$\bar{\rho}^{nd}_{M_L,M_L}=a^{(1/2)}_{M_L}+b^{(1/2)}_{M_L}\cos2\beta_2$

Coefficient	$M_L=0$	$\lvert M_L\rvert=1$	$\lvert M_L\rvert=2$
$a^{(1/2)}_{M_L}$	$\frac{1}{162}$	$\frac{1}{180}$	$\frac{1}{270}$
$b^{(1/2)}_{M_L}$	$\frac{1}{270}$	$\frac{1}{540}$	$-\frac{1}{270}$

$J_1=\frac{3}{2}$

$\bar{\rho}^{nd}_{M_L,M_L}=a^{(3/2)}_{M_L}+b^{(3/2)}_{M_L}\cos2\beta_1+c^{(3/2)}_{M_L}\cos2\beta_2+d^{(3/2)}_{M_L}\cos2\beta_1\cos2\beta_2$

Coefficient	$M_L=0$	$\lvert M_L\rvert=1$	$\lvert M_L\rvert=2$
$a^{(3/2)}_{M_L}$	$\frac{133}{10\,125}$	$\frac{1}{90}$	$\frac{181}{27\,000}$
$b^{(3/2)}_{M_L}$	$\frac{53}{6750}$	$\frac{2}{1125}$	$-\frac{43}{9000}$
$c^{(3/2)}_{M_L}$	$\frac{8}{1125}$	$\frac{19}{13\,500}$	$-\frac{109}{27\,000}$
$d^{(3/2)}_{M_L}$	$\frac{29}{6750}$	$-\frac{1}{300}$	$\frac{19}{9000}$

In the collision frame, we can calculate the multipole moments and alignment tensors from the diagonal elements of the *normalized* reduced time-averaged density matrix, which we now acknowledge as (relative) populations by defining

$$p_{M_L}(\Omega)\equiv\frac{\bar{\rho}^{nd}_{M_L,M_L}}{\mathrm{Tr}(\bar{\rho}^{nd})}\ , \tag{29}$$

where the argument $\Omega\equiv(\beta_1,\beta_2)$ denotes the functional dependence of these populations on polarizer angles. For example, the quadrupole alignment tensor for L, which is the quantum-mechanical analog of the classical quadrupole moment for a distribution of orbital angular-momentum vectors, is simply [21]

$$\begin{aligned}A_0^{(2)}&=\frac{\sqrt{6}}{\sqrt{L(L+1)}}\mathrm{Re}\langle L_0^{(2)}\rangle\\&=\frac{\sqrt{6}}{\sqrt{L(L+1)}}\sum_{M_L}(-1)^{L-M_L}p_{M_L}(\Omega)\\&\quad\times\begin{bmatrix}L&2&L\\-M_L&0&M_L\end{bmatrix}\langle L\|L^{(2)}\|L\rangle\ .\end{aligned} \tag{30}$$

The monopole tensor $A_0^{(0)}$, which is proportional to the total number of atoms in the Rydberg state, is just equal to 1. The quadrupole ($k=2$) and hexadecapole ($k=4$) tensors are

$$A_0^{(2)}=\sum_{M_L}\left[\frac{3M_L^2-6}{6}\right]p_{M_L}=2p_2-p_1-p_0\ , \tag{31a}$$

$$\begin{aligned}A_0^{(4)}&=\sum_{M_L}\left[\frac{72-155M_L^2+35M_L^4}{288}\right]p_{M_L}\\&=\tfrac{1}{12}(p_2-4p_1+3p_0)\ ,\end{aligned} \tag{31b}$$

where for clarity we have suppressed the dependence of the populations on $\Omega=(\beta_1,\beta_2)$ in these results. Analytical expressions for these quantities, based on the density matrix elements in Table III, are provided in Table IV.

Note that the quadrupole alignment tensor $A_0^{(2)}$ for excitation through $3\,^2P_{1/2}$ is independent of the angle β_1 of the polarization of the first laser, and the hexadecapole alignment tensor $A_0^{(4)}$ for this case is zero. This result obtains because the corresponding alignment tensor $A_q^{(k)}(\mathbf{J})$ for the *total* angular momentum $\mathbf{J}$ is zero unless $k\leq 2J$. Excitation via the second laser from $3\,^2P_{1/2}$ can only result in $n\,^2D_{3/2}$ states, so for this case $A_0^{(4)}(\mathbf{J})=0$ and hence the fourth-rank *orbital* alignment tensor (31b) is also zero. We shall examine these tensors further in the next section.

III. RESULTS

A. Total Rydberg-state populations

The trace of the (unnormalized) density matrix, Eq. (28), gives the total population in the *nd* state created by

TABLE IV. Simplified analytical expressions for the quadrupole ($k=2$) and hexadecapole ($k=4$) alignment tensors for two-step laser excitation of an *nd* state of Na through an intermediate $3\,^2P_{J_1}$ state with $J_1=\frac{1}{2}$ or $\frac{3}{2}$.

Alignment tensor	Expression
	$J_1=\frac{1}{2}$
$A_0^{(2)}$	$-\frac{7}{40}[1+3\cos2\beta_2]$
$A_0^{(4)}$	0
	$J_1=3/2$
$A_0^{(2)}$	$\frac{1}{25}\left[\frac{-439-777\cos2\beta_1-672\cos2\beta_2+132\cos2\beta_1\cos2\beta_2}{h(\beta_1,\beta_2)}\right]$
$A_0^{(4)}$	$\frac{9}{40}\left[\frac{1+7\cos2\beta_1+7\cos2\beta_2+17\cos2\beta_1\cos2\beta_2}{h(\beta_1,\beta_2)}\right]$
	where $h(\beta_1,\beta_2)\equiv79+3(\cos2\beta_1+\cos2\beta_2+\cos2\beta_1\cos2\beta_2)$

the two-step excitation. For $J_1=\frac{1}{2}$, this quantity is a number ($\frac{2}{81}$) independent of the polarizer angles β_1 and β_2. But as Table III and Fig. 3 show, for $J_1=\frac{3}{2}$ the trace depends on both angles. The importance of this finding for measurements such as the charge-transfer experiment (3) is that some polarizer-angle combinations are more efficient than others for exciting the *nd* state regardless of whatever alignments the two-step excitation may produce, a point to which we shall return in Sec. IV. The trace in Fig. 3 also exhibits fourfold symmetry about the point $(\beta_1,\beta_2)=(\pi/2,\pi/2)$.

The main utility of the trace of $\bar{\rho}^{nd}$, however, is in normalizing the density matrix to obtain the *fractional* populations of the magnetic sublevels of the *nd* state. In order to obtain the relative cross sections σ^{CT} in the charge-transfer experiments described in Sec. I one must "normalize" the collision signal by dividing by (among other things) a signal proportional to the number of target atoms in *nd* states. (This normalization signal is derived [31], in turn, from field ionization of the target atoms that remain after a few microseconds of exposure to the projectile beam.) In general both the numerator and denominator of Eq. (29) depend on the polarizer angles, so the dependence of p_{M_L} on these angles, although smooth, is more complicated than the simple sinusoidal dependence of the *absolute* sublevel populations given by the diagonal elements of the *unnormalized* density matrix, Eq. (26).

Figure 4 shows the fractional populations for each sublevel of the *nd* state as functions of β_1 and β_2 for $\beta_i=0$ to π. For $J_1=\frac{1}{2}$ these quantities, shown in Fig. 4(a), depend only on the second polarizer angle and exhibit symmetry about $\beta_2=0$ and $\pi/2$. For $J_1=\frac{3}{2}$ the populations depend on both polarizer angles, and Fig. 4(b) shows the symmetry about $\beta_i=0$ and $\pi/2$ that is inherent in the dependences of these populations on $\cos(2\beta_i)$ (see Table III). This figure appears to exhibit the same fourfold symmetry as the trace in Fig. 3, but in the full density matrix this symmetry is now only approximate. We shall consider this approximate symmetry in relation to experimental design in Sec. IV.

Another obvious feature of the populations for $J_1=\frac{1}{2}$ in Fig. 4(a) is the point of intersection of the three populations, the "magic angle" [44] at which

$$p_0(\Omega)=p_1(\Omega)=p_2(\Omega)=\tfrac{1}{5}\ . \tag{32}$$

In fact, because of the aforementioned symmetry about $\pi/2$ there are two such angles, $\beta_1=\cos^{-1}\sqrt{1/3}=54.7°$ and its complement.

The existence of magic angle(s) can be useful in the design of an experiment on the prepared Rydberg-state atoms because the resulting sublevel mixture is isotropic (unpolarized) only for such a magic-angle condition. For this special mixed state the density matrix is a multiple of the unit matrix, and the quadrupole and hexadecapole alignment tensors $A_0^{(2)}$ and $A_0^{(4)}$ vanish identically. Because the results of measurements at these special angles do not depend on orientations or alignments in the *nd*

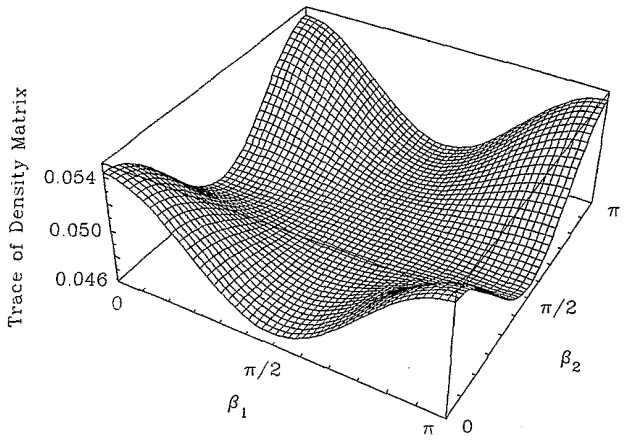

FIG. 3. The trace of the time-averaged density matrix for excitation of an *nd* Rydberg state of Na through the $3\,^2P_{3/2}$ intermediate state. The trace signifies the dependence on polarizer angles of the overall production of Rydberg atoms. For excitation through $3\,^2P_{1/2}$ the trace is angle independent.

states, these angles favor accurate replication of the experiment and facilitate quantitative comparisons between experimental and theoretical studies.

Although it is not readily apparent in the graphs of Fig. 4(b), investigation of the analytical forms for the density matrix for $J_1=\frac{3}{2}$ in Table III reveals that for excitation through $3\,^2P_{3/2}$ there are no exact magic-angle pairs, i.e., no angles (β_1,β_2) for which the resulting sublevel populations are equal. Figure 4(c) shows the varia-

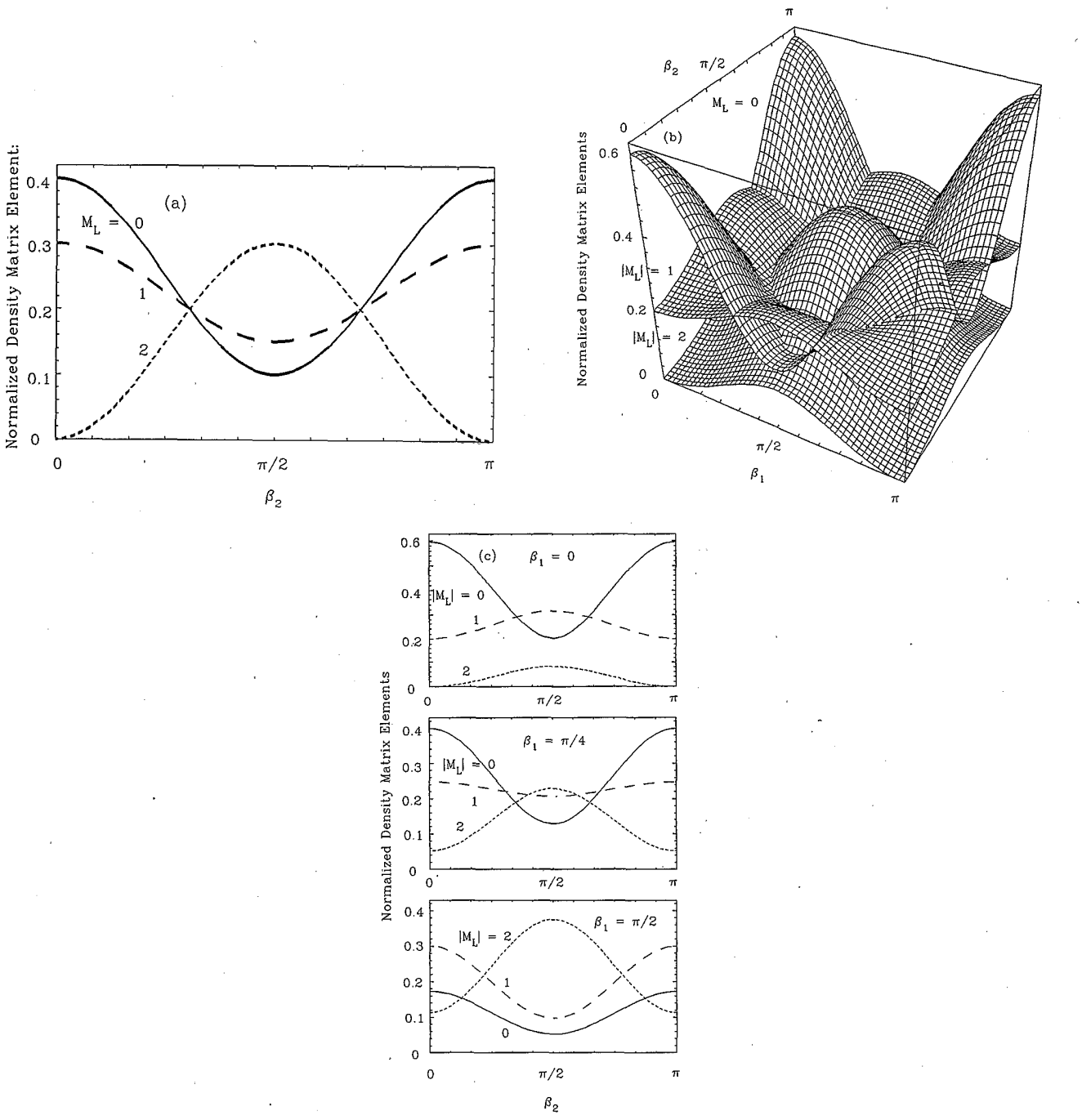

FIG. 4. Normalized diagonal elements of the time-averaged reduced density-matrix elements for excitation for an *nd* Rydberg state of sodium. These elements represent the fractional population of orbital magnetic sublevels of the Rydberg state. (a) For excitation through the $3\,^2P_{1/2}$ intermediate state, the matrix elements are independent of β_1 for each of the three sublevels: $|M_L|=0$ (solid curve), 1 (medium-dashed curve), and 2 (short-dashed curve). (b) For excitation through $3\,^2P_{3/2}$, however, they depend on both polarizer angles for $|M_L|=0$ (upper surface at corners of the figure), 1 (middle surface), and 2 (lower surface). These matrix elements manifest a slight departure from fourfold symmetry that can best be seen by comparing edges of the surfaces at $(\beta_1,\beta_2)=(0,\pi/2)$ and $(\pi/2,0)$. (c) Sectional views of the "quadrufoilar matriclopod" of (b) with first polarizer angle fixed at $\beta_1=0$, $\pi/4$, and $\pi/2$ and curves labeled as in (a).

tion of the fractional sublevel populations with β_2 for selected values of β_1. Near $\beta_1=\beta_2=19\pi/64$ the three sublevel populations become *nearly* equal: for $\beta_1=0.933\,599$ and $\beta_2=0.924\,416$ rad, we find $\bar{\rho}^{nd}_{0,0}=0.1929$, $\bar{\rho}^{nd}_{1,1}=0.2076$, and $\bar{\rho}^{nd}_{2,2}=0.1959$. (These angle pairs result from minimizing an algebraic expression which is quadratic in the pairwise differences between sublevel populations. Identical results are obtained at angles complementary to these.) At these "almost magic" angle pairs the sublevel populations are almost equal and the alignment tensors are small: $A_0^{(2)}=-0.0088$ and $A_0^{(4)}=-0.0046$. So the slight imbalance in sublevel populations at these angles is unlikely to reduce the usefulness of this configuration for experimental and theoretical comparison.

B. Absolute sublevel populations

To conclude our examination of sublevel populations, we show in Fig. 5 the *scaled* populations given by the diagonal elements of the *unnormalized* density matrix $\bar{\rho}^{nd}_{M_L,M_L}$ in (26). As noted above, these elements represent the actual, not fractional, populations from the two-step excitation of the *nd* Rydberg levels [45]. They therefore provide key information regarding excitation efficiency. For this reason we show for each M_L the populations for

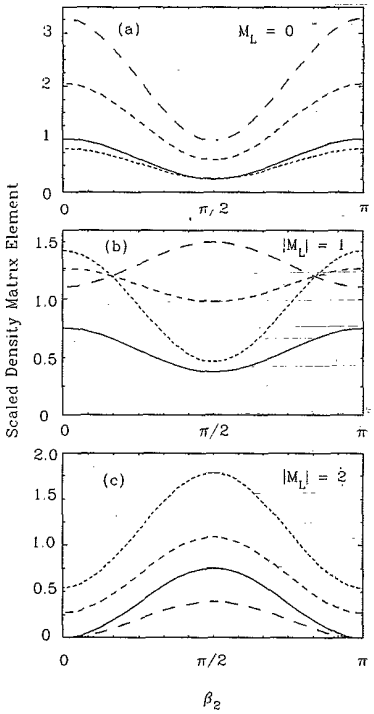

FIG. 5. Diagonal elements of the reduced time-averaged density matrix scaled so as to place excitation through the $3\,^2P_{1/2}$ and $3\,^2P_{3/2}$ states on the same scale. (a) For excitation through $3\,^2P_{1/2}$ (solid curve), the elements for $M_L=0$ are independent of β_1. For excitation through $3\,^2P_{3/2}$, we show results for $\beta_1=0$ (long-dashed curve), $\pi/4$ (medium-dashed curve), and $\pi/2$ (short-dashed curve). (b) Same as (a) for $|M_L|=1$ sublevels. (c) Same as (a) for $|M_L|=2$ sublevels.

both $J_1=\frac{1}{2}$ (which are independent of β_1) and for $J_1=\frac{3}{2}$ (at representative values of β_1). We have scaled the unnormalized elements in Table III to make the numerical values of these populations of order unity; specifically, we have divided them by $\bar{\rho}^{nd}_{0,0}(\beta_1=0,\beta_2=0;J_1=\frac{1}{2})$. We see, for example, that excitation of any of the M_L sublevels is more efficient if carried out through the $3\,^2P_{3/2}$ level except at selected values of β_2 for $M_L=0$ and 2.

C. Alignments

Using the fractional populations in Fig. 4 and the expressions in Table IV we have calculated the quadrupole and hexadecapole alignment tensors for $J_1=\frac{1}{2}$ [Fig. 6(a)] and for $J_1=\frac{3}{2}$ [Figs. 6(b) and 6(c)]. (As discussed in Sec. II, for excitation of $n\,^2D_{3/2}$ through the $3\,^2P_{1/2}$ state the hexadecapole tensor is zero.) These tensors must satisfy certain limits that follow from their definitions [21,37]. For $L=2$ these limiting conditions are

$$-1\le A_0^{(2)}\le 1,\quad -\tfrac{1}{6}\le A_0^{(4)}\le \tfrac{1}{2}\,. \tag{33}$$

Figure 6 shows that the calculated alignment tensors do indeed satisfy these inequalities. These figures also afford insight into the nature of the alignment produced by excitation at various polarizer angles. Thus $A_0^{(2)}$ is negative at angles where the ensemble of Rydberg states consists predominantly of atoms in the $M_L=0$ state and the orbital angular momentum is approximately normal to the z axis. By contrast, $A_0^{(2)}$ attains positive values near angles where the two-step excitation yields predominantly $M_L=\pm 2$ states. Similarly, $A_0^{(4)}$ attains its maximum (minimum) value when the predominantly $|M_L|=0(1)$ sublevels of the Rydberg atoms are occupied, respectively.

IV. EXPERIMENTAL DESIGN

One could use the density matrix elements derived in Sec. II and presented in Sec. III with the results of an experiment such as the charge-transfer experiment described in Sec. I to determine partial cross sections $\sigma^{CT}_{M_L}$ from measurements of the total charge-transfer cross section σ^{CT}. The latter quantity depends, of course, on the polarizer angles β_1 and β_2. In practice one would measure this cross section for a range of angle pairs (thereby varying the relative sublevel populations of the *nd* Rydberg state) and extract partial cross sections from the resulting data via a least-squares analysis. These cross sections would constitute parameters in a set of linear equations equal in number to N_p, the number of data points [angle pairs (β_1,β_2)] at which one measured σ^{CT}. If we denote a particular angle pair by an index i on the collective symbol Ω_i introduced in Eq. (29), then these equations have the form

$$\sigma^{CT}(\Omega_i)=p_0(\Omega_i)\sigma_0^{CT}+2p_1(\Omega_i)\sigma_1^{CT}+2p_2(\Omega_i)\sigma_2^{CT}\,,\qquad i=1,\ldots,N_p \tag{34}$$

where the relative populations $p_{M_L}(\Omega_i)$ are, according to Eq. (29), just the diagonal elements of the normalized

time-averaged reduced *nd* density matrix evaluated at Ω_i. The factors of 2 account for equal populations in $\pm M_L$ sublevels. Since Eq. (34) contains three unknowns, we must perform at least three distinct measurements to separate the three sublevel cross sections: i.e., the number of data points N_p must satisfy $N_p \geq 3$.

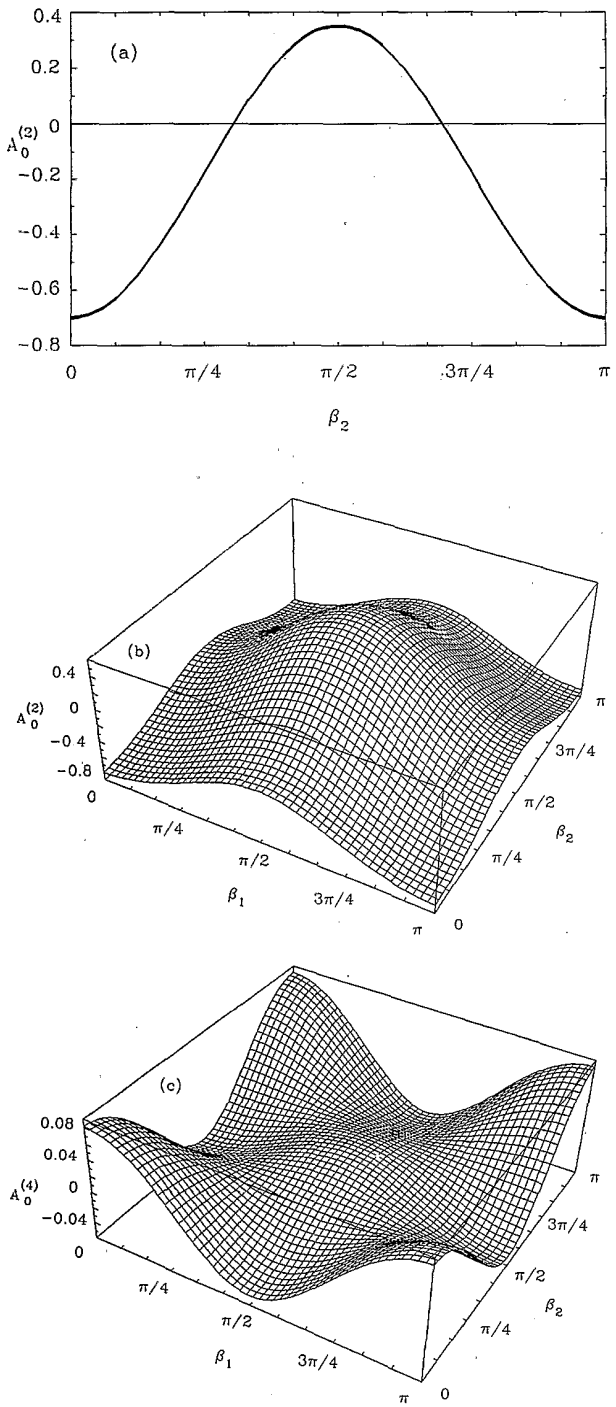

FIG. 6. The quadrupole orbital alignment $A_0^{(2)}$ (a) for excitation through the $3\,^2P_{1/2}$ state, which is independent of β_1, and (b) for excitation through $3\,^2P_{3/2}$, which depends on both polarizer angles. (c) The hexadecapole orbital alignment $A_0^{(4)}$ for excitation through $3\,^2P_{3/2}$, exhibiting its fourfold symmetry. For excitation through $3\,^2P_{1/2}$, this alignment is identically zero.

Beyond this, though, it is not obvious what constitutes an optimum experimental design. The complicated relationship of the populations $p_{M_L}(\Omega_i)$ to the polarizer angles (see Table III) makes it difficult to determine what design (i.e., what choice of points Ω_i) will produce the greatest distinction between the three partial cross sections. Two issues arise: first, at *how many* data points Ω_i should one measure σ^{CT} (that is, what is the optimum value of N_p) and *which* N_p angle pairs will maximize the accuracy of the partial cross sections? Second, how should one apportion the total measurement time T among the various Ω_i?

According to Poisson statistics the uncertainty of each measurement is proportional to the square root of the recorded charge-transfer signal f_i, and the relative uncertainty decreases with the time t_i spent in repeated measurements at the ith angle pair Ω_i as $t_i^{-1/2}$. But under stable measuring conditions the recorded signal f_i typically varies only slightly over the range of polarizer angles, so we can assume that the statistical weight σ_i^{-2} attached to the ith measurement is proportional to t_i irrespective of angles. The *fractional* time allotted to the ith angle pair is

$$\tau_i = \frac{t_i}{T} = \frac{t_i}{\sum_i^{N_p} t_i} , \tag{35}$$

and these τ_i may be taken as the weights of the individual measurements. A critical aspect of experimental design, then, is to decide how most efficiently to apportion the fixed time T among different choices for (β_1,β_2) by selection of corresponding τ_i.

The theory of design of least-squares experiments provides a mechanism to answer these questions [46]. First we construct from the populations $p_{M_L}(\Omega_i)$ the "design matrix" $\underline{A}$. This is a rectangular matrix whose three columns correspond to the three partial cross sections in Eq. (34). Each of the N_p rows of $\underline{A}$ corresponds to a data point, i.e., a polarizer angle pair (β_1,β_2). Second, we construct the normalized weight matrix $\underline{P}$, a diagonal $N_p \times N_p$ matrix of weights τ_i. The ith (diagonal) element of the weight matrix is just the inverse of the (normalized) variance for the measurements at Ω_i, i.e., $P_{i,i} = 1/\sigma_i^2$.

We then determine the optimum number and choice of data points Ω_i and apportionment of times T by maximizing the "design determinant"

$$D = \det \underline{A}^{\dagger} \underline{P} \, \underline{A} \ . \tag{36}$$

Doing so minimizes the volume of the hyperellipsoid of standard deviation in a least-squares fit of the N_p equations Eq. (34). Equation (36) can be put into a form that provides some insight into this method of optimizing experimental design. For a "minimal" experiment—i.e., one performed at just enough data points to allow solution of Eq. (34), in our case at $N_p = 3$ angle pairs—Eq. (36) reduces to

$$D = \left[\prod_{j=1}^{N_p} \tau_j \right] (\det \underline{A})^2 . \quad (37)$$

If the experiment is overdetermined so the number of data point exceeds the number of parameters, Eq. (36) can be expanded as

$$D = \sum_{\substack{i,j,k \\ (i>j>k)}} \tau_i \tau_j \tau_k \{\det([\underline{A}]_{ijk})\}^2 , \quad (38)$$

where $[\underline{A}]_{ijk}$ is the 3×3 matrix formed from the rows i,j,k of the design matrix $\underline{A}$ and the sum is carried out over all distinct choices $i<j<k$ from among the N_p rows of $\underline{A}$. We can therefore maximize the determinant D by concentrating the measurement time on those choices of polarizer angles which maximize as many of the matrices $[\underline{A}]$ as possible. This means, roughly, that we should select Ω_i to exhibit maximally contrasting contributions from the various populations p_{M_L}.

We have used this machinery to test a range of typical experimental designs. We first sought to decide whether it is preferable to perform a minimal experiment [e.g., spend equal time at three angle pairs, such as (0,0), $(0,\pi/2)$, and $(\pi/2,\pi/2)$] or to measure cross sections at angles chosen via a grid of values of (β_1,β_2) spaced by increments smaller than $\pi/2$. We defined grids of points $(i\pi/2n, j\pi/2n)$ in the (β_1,β_2) plane, where $n=1$, 2, 3, 6, 9, and 18, and $i,j=0,\ldots,n$. The structure of the density matrices shown in Fig. 4 suggests that the design determinants will be quite similar for sets of corresponding data points chosen from the upper or lower triangles defined by $\beta_2\geq\beta_1$ and $\beta_2\leq\beta_1$, respectively, shown in the inset in Fig. 7. For example, for $n=1$ (an angle increment of $\pi/2$) the design determinant for equally weighted data points drawn only from the upper triangle [(0,0), $(0,\pi/2)$, and $(\pi/2,\pi/2)$] is 24.07, larger but not dissimilar from the value 21.65 obtained for corresponding points in the lower triangle [(0,0), $(\pi/2,0)$, and $(\pi/2,\pi/2)$]; including all four data points corresponding to this increment, we obtain 19.40. By thus specifying angle increments $\pi/2$, $\pi/4$, $\pi/6$, $\pi/12$, $\pi/18$, or $\pi/36$, we define six grouped (square grid, upper-triangle, lower-triangle) *gedanken experiments* with, respectively, 3, 6, 10, 28, 55, and 190 points for the triangles (4, 9, 16, 49, 100, and 361 for the square grid) among which the total measuring time T is to be apportioned equally. The ordinate in Fig. 7 shows the cube root of the design determinant because in the present study this quantity is inversely related to the uncertainty for the three partial cross sections to be inferred via Eq. (34). Thus the quantity graphed in this figure is directly interpretable in terms of error bars.

In Fig. 7 we compare the design determinants for these prototypical experiments. We find that the optimal experimental design is to apportion T equally among the three data points in the upper triangle separated by $\pi/2$, i.e., at polarizer-angle pairs (0,0), $(0,\pi/2)$, and $(\pi/2,\pi/2)$. No experiment carried out at smaller angle increments comes close to being as efficient at determining the sublevel cross sections. Extensive studies of various uneven allocations of the total time T among data points for this and other prototype experiments failed to increase the design determinant, demonstrating that the symmetry suggested by Eq. (38) is, in fact, optimum: $\tau_1=\tau_2=\cdots=\tau_{N_p}$.

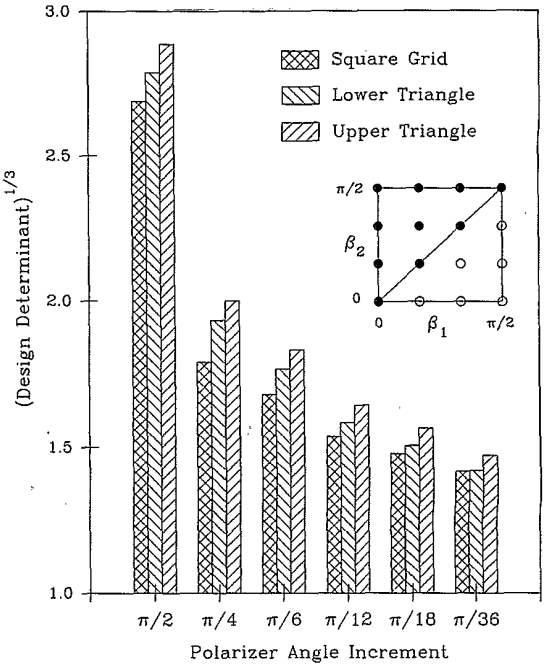

FIG. 7. The design determinants (cube root) for experiments using various polarizer-angle increments described in the text. "Lower triangle" refers to $\beta_2\leq\beta_1$ and "upper triangle" to $\beta_1\leq\beta_2$. "Square grid" designs cover the full range $\beta_1,\beta_2\in[0,\pi/2]$. The bars denote the relative capability of each design to separate the three sublevel partial cross sections $\sigma^{CT}_{M_L}$ by a least-squares fit of polarizer data as in Eq. (34). For each design the fixed total measurement time T is apportioned equally among the selected polarizer settings. The inset illustrates by solid dots the set of polarizer angles for an "upper triangle" experimental design with angle increment $\pi/6$.

It may nonetheless be desirable in practice to perform experiments using a smaller angle increment. A design that involves measurements only at polarizer angles 0 and $\pi/2$ gives no information about whether the signal variations in fact have the functional forms expected from the density matrix. In particular, such a choice would not reveal whether the signals are *even* functions of β_1 and β_2. An experimental asymmetry could result from misalignment of the polarizers, which would result in the incorrect inference of partial cross sections if it were not detected by a series of measurements at smaller angle increments. Figure 7 shows that choosing an increment smaller than $\pi/2$ does not greatly compromise the power of the experiment to distinguish between the partial cross sections and so would not limit the resulting insight into alignment effects for charge transfer.

V. DISCUSSION AND CONCLUSIONS

The formalism in Sec. II and results in Sec. III illustrate the use of density matrices and angular-momentum

analysis to relate the polarizations of laser beams to the distribution of atoms excited by those lasers among orbital sublevels of the final Rydberg state. Rather than attempt an encyclopedic study of all relevant experiments of this sort, we have worked through a single explicit, concrete example—two-step excitation of *nd* states of Na under common experimental conditions as described in Sec. II A—that is itself of significant interest. The analysis in Sec. IV gives one of several possible applications of this information: to optimizing design choices in setting up a charge-transfer experiment to determine partial cross sections as described in Sec. I.

In regard to this example, we have provided information concerning time-averaged sublevel populations of a Na(*nd*) Rydberg state in several forms.

(i) The density-matrix elements in a coupled angular momentum $\{|J_2M_2\rangle\}$ basis, which refers to sublevels of the *nd* fine-structure levels, appear in Eq. (21).

(ii) The diagonal elements of the reduced density matrix in an (uncoupled) orbital angular momentum $\{|LM_L\rangle\}$ basis are given in general form in Eq. (26), in simplified analytic form in Table III, and in (scaled) graphical form in Fig. 5. Up to a scaling factor that depends on experimental parameters ideally held constant, these diagonal elements are the populations of M_L sublevels.

(iii) The trace of the *nd* density matrix is given in general in Eq. (28), analytically in Table III, and graphically in Fig. 3. This quantity gives the variation of the *total* population of the *nd* Rydberg state with polarizer angles.

(iv) The diagonal elements of the normalized reduced density matrix are defined in Eq. (29) and illustrated in Fig. 4. These quantities represent the *fractional* population in any M_L sublevel of the *nd* state for polarizer angles (β_1,β_2).

(v) The quadrupole $A_0^{(2)}$ and hexadecapole $A_0^{(4)}$ alignments are defined in Eq. (31), given analytically in Table IV, and illustrated in Fig. 6. These alignment tensors reexpress information concerning the relative populations of the various magnetic sublevels in a spherical-tensor basis.

In especially simple cases (e.g., $\beta=0$ or $\pi/2$) one can work out the fractional populations in the *nd* state by more elementary methods than those employed here. Such an analysis has been performed previously by Jeys [47] and Jeys *et al.* [48] in a discussion of selective field ionization of Rydberg states of Na. The latter authors consider excitation of the Na(34*d*) state through the $3\,^2P_{1/2}$ intermediate state using collinear laser beams that propagate perpendicular to the axis of quantization $\hat{z}$. When a fast-rise (ionizing) electric-field pulse is applied to the Rydberg ensemble immediately following two-step laser excitation, the result is to project the $|JM_J\rangle$ fine-structure Rydberg states onto uncoupled $|LSM_LM_S\rangle$ states, a situation Jeys *et al.* refer to as diabatic passage to intermediate fields. As the ionizing field in their experiment further increases in strength, the Rydberg atoms in the various populated $|M_L|$ states give distinguishable selective-field-ionization signals; hence they analyze the projected populations in the orbital basis prior to ionization. Their simpler experimental geometry admits an analysis exclusively in terms of Clebsch-Gordan algebra. But their percentage populations, given in Table I of Ref. [48], should be identical to our p_{M_L} of Eq. (29).

In particular, the case Jeys *et al.* call "π polarization," corresponds to $\beta_2=0$ for $J_1=\frac{1}{2}$ in the present analysis. Their quoted populations: 40% for $M_L=0$, 60% for $|M_L|=1$, and 0% for $|M_L|=2$, indeed agree with our results in Fig. 4(a), where $p_0=0.4$ and $2p_1=0.6$.

The case Jeys *et al.* call "σ polarization," with excitation through $3\,^2P_{1/2}$ in a collinear geometry, is not precisely the same as any in our mutually perpendicular geometry. For the present experimental arrangement shown in Fig. 2, when $\beta_1=\beta_2=\pi/2$, the electric-field directions of the two lasers are perpendicular to each other, while in the σ case of Ref. [48] they are parallel. But we can compare to their results for $J_1=\frac{1}{2}$, since as shown in Table III, the fractional populations for this intermediate state are independent of β_1 and so our results for $\beta_2=\pi/2$ should be identical to theirs. Indeed, the percentages quoted in Ref. [48] for $|M_L|=0$, 1, and 2 agree with the population $p_0=0.1$, $2p_1=0.3$, and $2p_2=0.6$ in Fig. 4(a).

Although excitation through the $3\,^2P_{3/2}$ state is not discussed in [48], it is addressed in an Appendix to Jeys [47]. From the latter reference we determined the time-averaged probabilities for two-step laser excitation in which the electric-field vectors of both lasers are parallel to the z axis as $\frac{111}{275}$, $\frac{164}{275}$, and zero for $M_L=0$, 1, and 2, respectively. These predictions agree precisely with ours as inferred from Table III and given numerically in Fig. 4(c).

Finally, we note that the observation of Jeys *et al.* of their predicted populations of 10% for $M_L=0$ and 60% for $|M_L|=2$ in field ionization after a sufficiently rapid passage to intermediate fields (see their Fig. 3) verifies the insignificance of hyperfine effects in their experiment. This observation, in turn, corroborates our assumption (in Sec. II A) that hyperfine precession in the $3\,^2P_{1/2}$ state does not affect the outcome for an excitation process whose timing is similar to those considered in Sec. I.

Applying the methods of this paper to other atoms or excitation schemes would require in most cases some modifications in the formulation, for example, to accommodate ground states with $L>0$ or spin multiplicities other than doublet, hyperfine effects, quantum beats in time-resolved experiments, circular polarization, and different beam propagation geometries. We hope that the details of the present analysis will guide the description of other cases using density-matrix and tensorial methods.

ACKNOWLEDGMENTS

The authors would like to thank C. H. Greene for helpful discussions and encouragement. Most of this work was done while the authors were supported by the JILA Visiting Fellowship Program, and we are grateful to the University of Colorado at Boulder and NIST for their support and hospitality. This work was supported in part by NSF Grants No. PHY-9122377 and PHY-9108890.

*Permanent address: Department of Physics & Astronomy, University of Kentucky, Lexington, KY 40506-0055.
†Permanent address: Department of Physics & Astronomy, University of Oklahoma, Norman, OK 73019-0225.

[1] S. Haroche, M. Gross, and M. P. Silverman, Phys. Rev. Lett. **33**, 1063 (1974).
[2] T. W. Ducas, M. G. Littman, R. R. Freeman, and D. Kleppner, Phys. Rev. Lett. **35**, 366 (1975).
[3] T. F. Gallagher, L. M. Humphrey, R. M. Hill, W. E. Cooke, and S. A. Edelstein, Phys. Rev. A **15**, 1937 (1975).
[4] *Rydberg States of Atoms and Molecules,* edited by R. F. Stebbings and F. B. Dunning (Cambridge University Press, New York, 1983).
[5] C. Fabre, S. Haroche, and P. Goy, Phys. Rev. A **18**, 229 (1978); **22**, 778 (1980).
[6] L. G. Gray, X. Sun, and K. B. MacAdam, Phys. Rev. A **38**, 4985 (1988).
[7] T. F. Gallagher, S. A. Edelstein, and R. M. Hill, Phys. Rev. Lett. **35**, 644 (1975); Phys. Rev. A **15**, 1945 (1977).
[8] K. B. MacAdam, D. A. Crosby, and R. Rolfes, Phys. Rev. Lett. **44**, 980 (1980).
[9] L. J. Wang, M. King, and T. J. Morgan, J. Phys. B **19**, L623 (1986).
[10] K. B. MacAdam, in *Atomic Physics 12,* edited by J. C. Zorn and R. R. Lewis (AIP, New York, 1991), p. 310.
[11] X. Ling and K. A. Smith, Phys. Rev. A **47**, R1 (1993).
[12] B. D. DePaola (private communication).
[13] S. Haroche and D. Kleppner, Phys. Today **42** (1), 24 (1989).
[14] S. Haroche, M. Brune, and J. M. Raimond, in *Atomic Physics 12* (Ref. [10]), p. 204.
[15] G. Alber and P. Zoller, Phys. Rep. **199**, 231 (1991).
[16] P. M. Koch, *The Ubiquity of Chaos,* edited by S. Krasner (AAAS, Washington, DC, 1990), p. 75.
[17] R. G. Hulet and D. Kleppner, Phys. Rev. Lett. **51**, 1430 (1983).
[18] J. Hare, M. Gross, and P. Goy, Phys. Rev. Lett. **61**, 1938 (1988).
[19] J. Macek and D. H. Jaecks, Phys. Rev. A **4**, 2288 (1971).
[20] M. Eminyan, K. B. MacAdam, J. Slevin, and H. Kleinpoppen, J. Phys. B **7**, 1519 (1974).
[21] R. N. Zare, *Angular Momentum: Understanding Spatial Aspects in Chemistry and Physics* (Wiley, New York, 1988).
[22] J. J. McClelland, S. R. Lorentz, R. E. Scholten, M. H. Kelley, and R. J. Celotta, Phys. Rev. A **46**, 6079 (1993).
[23] C. J. Smith, J. P. J. Driessen, L. Eno, and S. R. Leone, J. Chem. Phys. **96**, 8212 (1992).
[24] R. Hippler, J. Phys. B **26**, 1 (1993).
[25] O. Yenen, D. H. Jaecks, and P. J. Martin, Phys. Rev. A **35**, 1517 (1987).
[26] U. Fano and J. H. Macek, Rev. Mod. Phys. **45**, 553 (1973).
[27] M. Eminyan, K. B. MacAdam, J. Slevin, and H. Kleinpoppen, Phys. Rev. Lett. **31**, 576 (1973).
[28] I. V. Hertel and W. Stoll, J. Phys. B **7**, 570 (1974); **7**, 583 (1974).
[29] N. Andersen, J. W. Gallagher, and I. V. Hertel, Phys. Rep. **165**, 1 (1988).
[30] N. Andersen (private communication).
[31] K. B. MacAdam, L. G. Gray, and R. G. Rolfes, Phys. Rev. A **42**, 5269 (1990).
[32] S. B. Hansen, L. G. Gray, E. Horsdal-Pedersen, and K. B. MacAdam, J. Phys. B **24**, L315 (1991).
[33] J. C. Houver, D. Dowek, C. Richter, and N. Andersen, Phys. Rev. Lett. **68**, 162 (1992).
[34] Z. Roller-Lutz, Y. Wang, K Finck, and H. O. Lutz, Phys. Rev. A **47**, R13 (1993).
[35] K. Blum, *Density Matrix Theory and Applications* (Plenum, New York, 1981).
[36] D. ter Haar, Rep. Prog. Phys. **24**, 304 (1961).
[37] C. H. Greene and R. N. Zare, J. Chem. Phys. **78**, 6741 (1983).
[38] E. Arimondo, M. Inguscio, and P. Violino, Rev. Mod. Phys. **49**, 31 (1977).
[39] T. H. Jeys, K. A. Smith, F. B. Dunning, and R. F. Stebbings, Phys. Rev. A **23**, 3065 (1981).
[40] L. Allen and J. H. Eberly, *Optical Resonance and Two-Level Atoms* (Dover, New York, 1987).
[41] W. R. MacGillivray and M. C. Standage, Comments At. Mol. Phys. **26**, 179 (1991).
[42] B. L. Silver, *Irreducible Tensor Methods* (Academic, New York, 1976).
[43] D. A. Varshalovich, A. N. Moskalev, and V. K. Khersonskii, *Quantum Theory of Angular Momentum* (World Scientific, Singapore, 1988).
[44] B. L. Moiseiwitsch and S. J. Smith, Rev. Mod. Phys. **40**, 238 (1968).
[45] The overall constant that relates these tabulated matrix elements to the actual number of Na(nd) atoms in an experiment depends on laser intensity, pulse length, detuning, line shape, beam size and overlap, Na vapor density, atomic radial dipole matrix elements, and fundamental constants. This constant is therefore independent of angles and quantum numbers and hence irrelevant to the present discussion.
[46] W. C. Hamilton, *Statistics in Physical Science: Estimation, Hypothesis Testing, and Least Squares* (Ronald, New York, 1964).
[47] T. H. Jeys, Ph.D. dissertation, Rice University, 1982 (unpublished).
[48] T. H. Jeys, G. B. McMillian, K. A. Smith, F. B. Dunning, and R. F. Stebbings, Phys. Rev. A **26**, 335 (1982).